

# *In Situ* Microfabrication and Measurements of Bi<sub>2</sub>Se<sub>3</sub> Ultrathin Films in a Multichamber System with a Focused Ion Beam, Molecular Beam Epitaxy, and Four-Tip Scanning Tunneling Microscope

Naoya Fukui,\* Rei Hobara, Toru Hirahara,† and Shuji Hasegawa

Department of Physics, University of Tokyo, 7-3-1 Hongo, Bunkyo-ku, Tokyo 113-0033, Japan

Yutaka Miyatake, Hiroyuki Mizuno, Toru Sasaki, and Toshihiko Nagamura

UNISOKU Co., Ltd., 2-4-3, Kasugano, Hirakata, Osaka 573-0131, Japan

(Received 18 July 2014; Accepted 26 September 2014; Published 11 October 2014)

Ultrathin films of Bi<sub>2</sub>Se<sub>3</sub> grown on Si(111) substrate were etched into submicron-width wires by using a focused ion beam (FIB), and their electrical resistance was measured using the four-probe method with a four-tip scanning tunneling microscope. All of the procedures were performed *in situ* in ultrahigh vacuum without exposing the sample to air. One-dimensional conduction of the films was confirmed from the dependence of the resistance on the length of wire under measurement, meaning that successful lossless current path control laterally as well as vertically can be obtained with FIB etching. Protecting the sample surface from unintentional gallium ion beam irradiation in the FIB process was also found to be important for maintaining the intrinsic electrical properties of the Bi<sub>2</sub>Se<sub>3</sub> films. [DOI: 10.1380/ejssnt.2014.423]

Keywords: Electrical transport measurements; Multiprobe method; Scanning Tunneling Microscopy; Ion etching; Focused ion beam

## I. INTRODUCTION

Surface electronic states, localized at well-defined crystal surfaces, have been intensively investigated with various kinds of surface science techniques, such as angle-resolved photoelectron spectroscopy (ARPES), scanning tunneling microscopy (STM), and scanning tunneling spectroscopy (STS). These studies so far have revealed many interesting surface systems owing to intrinsic low-dimensionality and broken space-inversion symmetry, showing surface charge-density-wave systems[1–3], surface Rashba systems[4–6], topological surface states[7–9], and other phenomena. In light of not only basic science but also possible device applications, the surface is now regarded as one of the important material phases, because surface/edge contributions to physical properties should increase as the size of electronic devices becomes smaller. Therefore, it is important to investigate the electronic transport characteristics of surface/edge states.

*In situ* four-point probe methods in ultrahigh vacuum (UHV) have been used to measure the electrical properties of surface states [10–15]. It is crucial to measure the properties *in situ* without exposing the sample surfaces to air to keep the surfaces clean and well defined. Such sample surfaces in many cases were prepared uniformly on a substrate of millimeter size, and the electric current was made to flow and spread on the surface laterally without any restriction. In several studies, however, the current path was restricted with a processed substrate[16, 17]. Tegenkamp *et al.* successfully controlled the direction of current and revealed the difference in resistivity between directions parallel to and perpendicular to the atomic chains of the Pb/Si(557) surface [16]. In this experiment, the substrate was submillimeter in size. When sample size is reduced below representative

lengths of the electronic system under investigation, such as the mean free path of carriers and the spin diffusion length, by restricting the current path, we can explore further new aspects of surface-state transport. Nevertheless, there have been few studies on surface-state electrical conduction limited to areas smaller than the micrometer scale. Heike *et al.*[11] obtained STM topographic images of a nanostructure shaped by scratching a Si(111)-7 × 7 surface with an STM tip and estimated its surface conductivity. Although the electrical resistance was not explicitly measured, it was estimated from the contrast in STM images.

One approach to this issue is to combine a four-tip STM for four-probe electrical measurements with a focused ion beam (FIB) technique for microfabrication of surfaces. Since FIBs do not need a chemical process, *in situ* fabrication can be done in UHV. In the FIB technique, charged ions (most often Ga<sup>+</sup>) are electromagnetically accelerated up to tens of kilovolts and focused into nanometer diameters. The focused ions sputter atoms off the surface of a sample to make dips, trenches [18], and even complex and functional patterns [19]. Such FIB etching is a possible technique for restricting the current path in intentional ways to investigate the electrical properties of *surface systems with boundaries*.

We have developed a multichamber UHV system that fulfills all the requirements mentioned above, using molecular beam epitaxy (MBE) for preparing well-defined sample surfaces and epitaxial films, FIBs for patterning, and four-tip STM for electrical measurements, all of which are connected to each other with vacuum tunnels. However, it is not obvious whether such FIB-patterned surfaces show the intrinsic transport properties of surface states.

In this work, Bi<sub>2</sub>Se<sub>3</sub> ultrathin films, one type of topological materials, were grown epitaxially on Si(111) substrate, and then wires of width down to 400 nm were fabricated from the film by the *in situ* FIB method. Finally, their resistance was measured with a four-tip STM. It was shown that the Bi<sub>2</sub>Se<sub>3</sub> film was successfully etched into submicron wires by confirming the one-dimensional

\* Corresponding author: fukui@surface.phys.s.u-tokyo.ac.jp

† Present address: Department of Physics, Tokyo Institute of Technology, 2-12-1 Ookayama, Meguro-ku, Tokyo 152-8551, Japan

electrical conduction through them. We also found that the bare  $\text{Bi}_2\text{Se}_3$  film was sensitive to unintentional irradiation of the  $\text{Ga}^+$  beam (probably owing to the beam tail extending out from the beam center) in the FIB process; its conductivity was easily reduced by damage caused by the irradiation. It was important to cover the film with a capping material during FIB etching to avoid damage and maintain the film's intrinsic properties.

## II. INSTRUMENTAL DETAILS

Figure 1(a) shows a photograph of the multichamber system we have developed, and Fig. 1(b) shows its top-view drawing. The system consists of four chambers: a load-lock chamber, a preparation chamber for MBE, a FIB chamber, and a four-tip STM chamber. All four chambers are at a base pressure  $< 10^{-7}$  Pa and are connected to each other by vacuum tunnels with gate valves. STM tips and samples were introduced via the load-lock chamber and transferred from one chamber to another. The whole system was placed on an antivibration table working by compressed air. MBE and reflection high-energy electron diffraction (RHEED) were available in the preparation chamber so that *in situ* observations of surface structure and film growth can be performed. A UHV-type FIB column (Magnum, FEI Company) was attached to the FIB chamber. When FIB processing was performed, a sample was mounted on a four-axis-goniometer stage (horizontal  $X$  and  $Y$  motions and polar and azimuth rotations). The four-tip STM chamber was equipped with a UHV-type scanning electron microscope (SEM) column (two-lens Schottky emission electron focusing column, FEI Company) on top to navigate the four tips to the aimed positions on the sample surface. Four sets of STM units, which are driven electrically by stacked piezoelectric ceramics, were installed in a cooling system (Figs. 1(c)(d)). The cooling system is revised from the previous four-tip STM system[20] to attain lower temperatures. It consists of an outer tank (for liquid  $\text{N}_2$ ), an inner tank (for liquid He), and a 1 K pot. Liquid helium is pulled up to the 1 K pot from the inner tank by pumping the pot, reaching 3.6 K on the sample stage. However, the electrical measurements shown here were done only at room temperature.

## III. EXPERIMENTS

### A. Insulating Trench

To restrict and control the current paths on the surfaces of thin films, we need to fabricate insulating trenches having sufficiently high resistance. We first confirmed the etching conditions in FIB fabrication of insulating trenches in a  $\text{Bi}_2\text{Se}_3$  film grown on Si(111) substrate.

A silicon substrate of  $15 \times 3 \text{ mm}^2$  was cut out of a Si(111)  $n$ -type (P-doped) wafer with resistivity  $> 1000 \Omega \text{ cm}$  at room temperature. A clean Si(111)- $7 \times 7$  surface superstructure was obtained after a cycle of resistive heat treatments in UHV. Then, one monolayer (ML) of bismuth ( $1 \text{ ML} = 7.8 \times 10^{14} / \text{cm}^2$ , the atom density of the

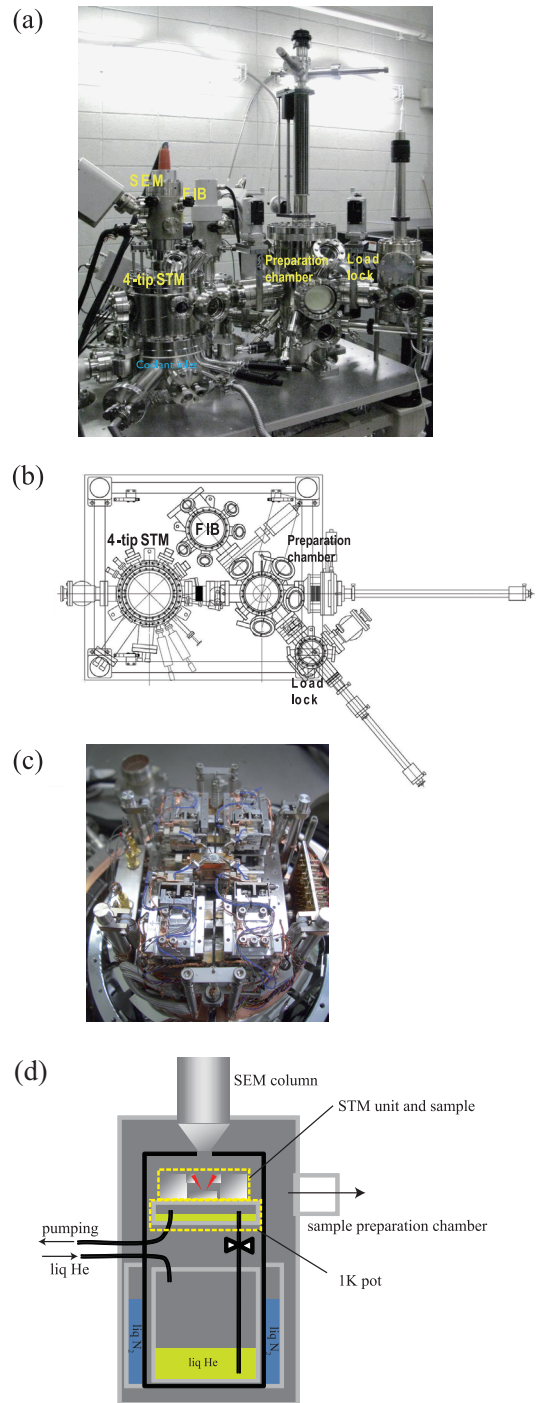


FIG. 1. (a) Photograph and (b) top-view drawing of the multichamber system. (c) Photograph of the four-tip STM stage. (d) Illustration of the cooling system in the four-tip STM chamber.

Si(111) topmost surface) was deposited to form a Si(111)- $\beta\sqrt{3} \times \sqrt{3}$ -Bi surface superstructure, so that an epitaxial  $\text{Bi}_2\text{Se}_3$  film with high quality can be grown on it [21]. An 8-quintuple-layer-thick  $\text{Bi}_2\text{Se}_3$  film was prepared by co-depositing Bi and Se with the ratio of 1:10 onto the  $\beta\sqrt{3} \times \sqrt{3}$ -Bi surface kept at  $150^\circ\text{C}$ . The RHEED pattern shown in Fig. 2(a) [22] was taken from this film surface, indicating a flat and high-quality single-crystalline film grown. Before the FIB etching, a Se capping layer of 20–30 nm thick was deposited onto the  $\text{Bi}_2\text{Se}_3$  surface

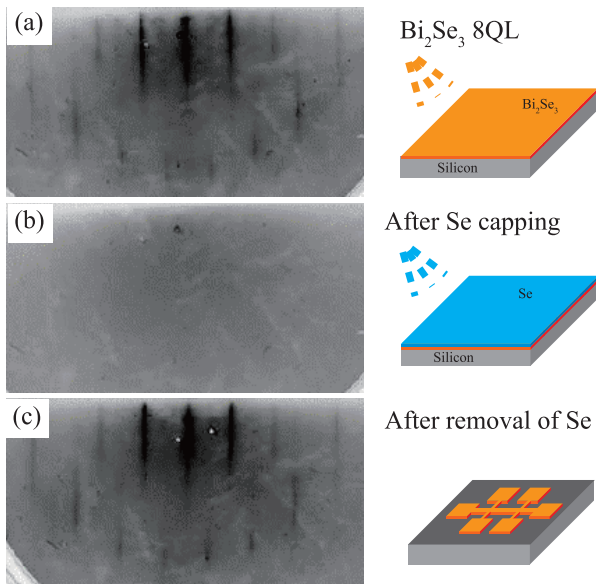


FIG. 2. RHEED pattern of an 8-quintuple-layer-thick Bi<sub>2</sub>Se<sub>3</sub> film grown on Si(111) substrate, (a) right after the MBE growth, (b) after deposition of a Se capping layer on it, and (c) after removal of the Se capping layer by heating. The illustrations correspond to those in Fig. 4.

at room temperature (to protect the surface from unintentional irradiation of the Ga<sup>+</sup> beam as described below). The RHEED pattern shows no spots, as shown in Fig. 2(b), indicating that an amorphous layer of Se was grown. After FIB patterning, the sample was heated to 150°C to remove the Se layer, resulting in the RHEED pattern of Fig. 2(c) (taken from a surface area outside of the patterned area on the sample), which was the same as in (a), indicating recovery of the bare Bi<sub>2</sub>Se<sub>3</sub> surface.

First, a rectangular island of 15 × 20 μm<sup>2</sup> was isolated from the surrounding area of the Bi<sub>2</sub>Se<sub>3</sub> film by a wide trench drawn by a 330-pA Ga<sup>+</sup> beam with 20 times repeated scanning (gray area in the insets of Fig. 3). Then a narrow trench was drawn to bisect the rectangular island of Bi<sub>2</sub>Se<sub>3</sub> film. The narrow trench was drawn by lower Ga<sup>+</sup> currents (1, 7.5, and 50 pA) with a controlled total amount of Ga<sup>+</sup> dose at each position (by changing the irradiation duration at each position). The resistance between the bisected parts of the Bi<sub>2</sub>Se<sub>3</sub> film island was measured across the narrow trench by using the four-probe method, as shown in the inset of Fig. 3.

The measured resistances are shown in Fig. 3 as a function of the total amount of Ga<sup>+</sup> ion dose per unit area in the trench. At a dose of 1.4 × 10<sup>16</sup> ions/cm<sup>2</sup>, the lowest dose in this study, the resistance is 6 kΩ, whereas it increases abruptly to a few MΩ above the dose of ≈3.6 × 10<sup>16</sup> ions/cm<sup>2</sup>. It is natural to consider that the Bi<sub>2</sub>Se<sub>3</sub> film is sputtered sufficiently by this amount of Ga<sup>+</sup> beam irradiation to make a sufficiently insulating trench. This threshold amount of Ga<sup>+</sup> dose roughly corresponds to the number of dosed Ga<sup>+</sup> ions comparable to that of the Bi and Se atoms lying in the irradiated area. The threshold also coincides with the value where FIB starts removing surface atoms instead of swelling the surface in a silicon crystal [23]. The resistance gradually increases with further dose above the threshold one, indicating that some

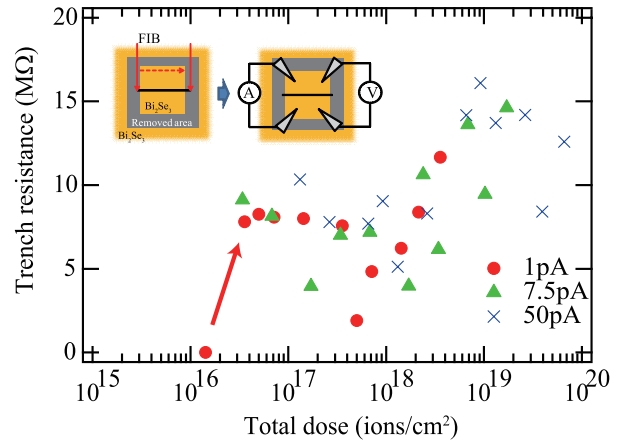


FIG. 3. Resistance across the trench in Bi<sub>2</sub>Se<sub>3</sub> film as a function of the dose of Ga ions at each position during the FIB fabrication. The red circles, green triangles, and blue crosses correspond to 1, 7.5, and 50-pA Ga<sup>+</sup> beam currents in FIB, respectively. By repeating the beam scan along the trench, the total dose of Ga<sup>+</sup> was changed. The red arrow emphasizes the drastic change of the trench resistance. The insets show the sample and measurement method.

additional effect such as widening of the trench is caused by the excess dose. In this work, in fabricating wire structures on the Bi<sub>2</sub>Se<sub>3</sub> film described below, trenches were fabricated with a dose of 5.0 × 10<sup>16</sup> ions/cm<sup>2</sup>.

### B. Bi<sub>2</sub>Se<sub>3</sub> Wires

The insulating trenches thus fabricated under the conditions mentioned above should serve as boundaries to restrict the current path on the Bi<sub>2</sub>Se<sub>3</sub> film surface. We fabricated Bi<sub>2</sub>Se<sub>3</sub> wires from the Bi<sub>2</sub>Se<sub>3</sub> film grown on Si(111) substrate and controlled the current path by using the insulating trenches. Furthermore, we also investigated the influence of Ga<sup>+</sup> irradiation in the FIB on the resistance of the film and wires.

A Bi<sub>2</sub>Se<sub>3</sub> film was prepared in the same manner as mentioned in the previous section. To determine the influence of unintentional Ga<sup>+</sup> irradiation, we prepared two types of samples, as shown in Fig. 4; one was etched by a FIB with a Se capping layer deposited on the Bi<sub>2</sub>Se<sub>3</sub> film, and another was etched without the capping layer. For the Se-capped sample, a 20-30-nm-thick amorphous Se layer was deposited onto the Bi<sub>2</sub>Se<sub>3</sub> film, as much as the zeroth Laue spots of Bi<sub>2</sub>Se<sub>3</sub> in RHEED pattern completely disappeared (Fig. 2(b)). After the sample was covered with Se, it was etched by using the FIB into a fine structure in the shape of a Hall bar (Figs. 5(a) and (b)).

The Hall bar consists of three parts: a wire under measurement, having a constant width  $w$  (=0.4–6.0 μm), pads for tip contact, and leads connecting the pads with the wire. The tip-contact pads are for avoiding possible damage of the wire by the direct contact of tips (as reported in Ref. 24).

We employed two types of insulating trenches fabricated by using different etching conditions (Table I): *outline trenches* and *fine trenches*. The outline trenches were used for outlining the pads and leads, which were fabri-

TABLE I. The FIB etching parameters used in the present experiments. The dwell time is how long the beam stays at a position before moving to a neighboring position. The distance between the two points is the beam interval. The beam diameter is defined as the full width at half maximum of the beam intensity profile, which has a Gaussian distribution.

	outline trenches	fine trenches
Beam current (pA)	370	1
Dwell time ( $\mu\text{s}$ )	7000	350
Beam interval (nm)	50	12.5
Beam diameter (nm)	40	7
Repetition	1	20

cated by using a high ion current in the FIB; the dwell time (irradiation duration of the  $\text{Ga}^+$  beam at each position) and the beam current were set to be 7000  $\mu\text{s}$  and 370 pA, respectively. The insulating regions that isolate the Hall bar pattern from the surrounding area were formed by meshes of the outline trenches at 1- $\mu\text{m}$  interval (Fig. 5(a)). The fine trenches, bordering the wire under measurement (Fig. 5(b)), were fabricated by the lower ion current (1 pA), as shown in Table I, to obtain better resolution and to minimize the irradiation damage near the trenches. Moreover, the scanning of the  $\text{Ga}^+$  beam was repeated 20 times for the fine trenches to obtain a smoother shape and sufficient insulating property. For comparison, the trenches bordering the  $\text{Bi}_2\text{Se}_3$  wire on some samples were fabricated by using a higher ion current of 330 pA to allow us to discern the influence of the intensity of the FIB beam on the edge of wire.

The wire has five branches of leads every 10  $\mu\text{m}$ . Both ends of the wire were also connected to pads, which are used for injecting current (see the inset of Fig. 4). After the FIB etching, the Se layer was removed by 150°C Joule heating by a current fed through the clamps at both ends of Si substrate. We confirmed that the  $\text{Bi}_2\text{Se}_3(111)$  bare surface was recovered by the heating, as observed by RHEED shown in Fig. 2(c).

We also prepared another type of  $\text{Bi}_2\text{Se}_3$  sample that were etched without the Se capping layer during FIB fabrication (Fig. 4). In addition, a 20-bilayer-thick Bi sample was prepared for comparison to  $\text{Bi}_2\text{Se}_3$  samples. The Bi film was deposited on a Si(111)-7  $\times$  7 surface at room temperature and etched by a 330-pA FIB without any capping materials.

A scanning electron microscope image of a  $\text{Bi}_2\text{Se}_3$  wire is shown in Fig. 5(a). The light-gray regions are the pristine  $\text{Bi}_2\text{Se}_3(111)$  surface, whereas the dark areas are the regions etched by the FIB. The wire under measurement lies horizontally in the middle of the image, enclosed by the white dashed lines. A scanning ion microscope (SIM) image of the wire is shown in Fig. 5(b). This image was taken after all electrical measurements were done because ion irradiation during SIM observation seriously damages the films. It is also noticed that the contrast in (b) is reversed compared with the SEM image in (a); the dark gray areas in (b) are the pristine  $\text{Bi}_2\text{Se}_3$  regions, whereas the brighter areas are the FIB-etched regions. In the configuration of the four tips as shown in Fig. 5(a), the re-

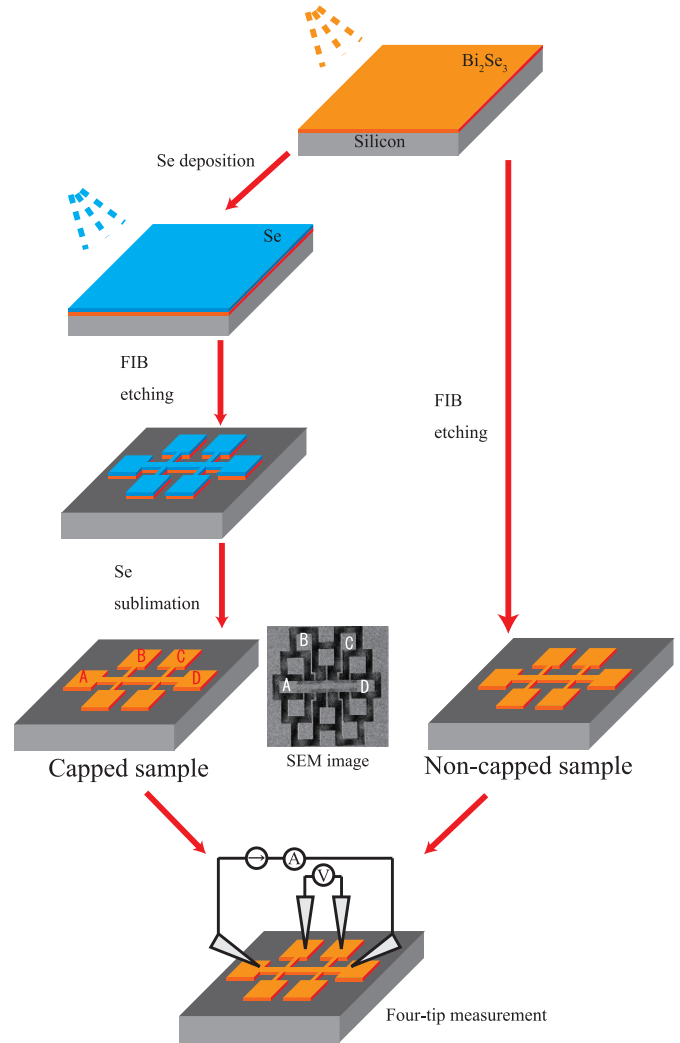


FIG. 4. Illustration showing the procedure for making the Hall bar structures out of  $\text{Bi}_2\text{Se}_3$  film. The gray regions indicate the insulating regions made by the FIB etching. The yellow and blue areas are  $\text{Bi}_2\text{Se}_3$  and Se layers, respectively. The inset is an SEM image ( $112 \times 112 \mu\text{m}^2$ ) of the patterned structure. The correspondence between the schematic picture and the SEM image of a fine structure is shown by the letters A, B, C, and D.

sistance of a 1- $\mu\text{m}$ -wide wire is measured with a probe spacing of 20  $\mu\text{m}$ .

Before the measurements of the wires, we measured the sheet conductivity of the pristine  $\text{Bi}_2\text{Se}_3$  film by the four-point probe method. Because the measured area (unpatterned area) on the film was about 1 mm away from the FIB-patterned area, the influence of the  $\text{Ga}^+$  beam irradiation should be negligible. The four tips were aligned on a line with equal spacing  $s$  on the  $\text{Bi}_2\text{Se}_3$  film (i.e., linear four-point probe method was used). The result is shown in Fig. 6(a) as a function of  $s$ . Here, the resistance  $R$  is defined as the voltage drop between the tips 4 and 3 divided by the current flowing from tips 1 to 2, as shown in the inset of Fig. 6(a). We fitted the resistances against  $s$  with two types of curves: two-dimensional conduction ( $R \propto s^0$ , the black dashed line in Fig. 6(a)) and three-dimensional conduction ( $R \propto s^{-1}$ , the blue dashed line). Since the resistance is almost constant irrespective of  $s$  rather than proportional to  $1/s$ , one can say that

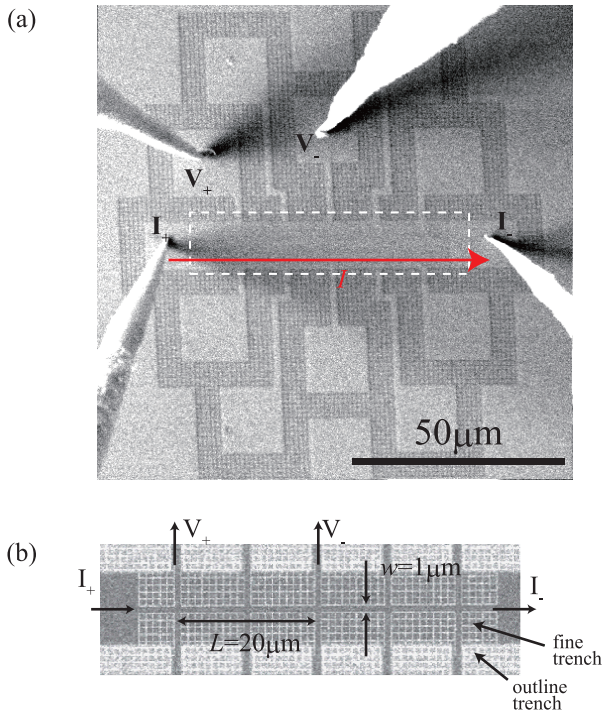


FIG. 5. (a) SEM image of the Hall bar structure under measurement with the four tungsten tips attached to the contact pads. The SEM acceleration voltage was 12 kV. The current is made to flow from the  $I_+$  tip to the  $I_-$  tip for resistance measurement. The voltage between the  $V_+$  tip and the  $V_-$  tip is measured. (b) SIM image of the region surrounded by the white dashed line in (a). The SIM acceleration voltage was 30 kV, with a beam current of 1 pA. The fine trench and outline trench regions are shown by the arrows. The outline trenches look brighter than the fine trenches.

this is a two-dimensional conduction [25]. Therefore, the measured resistance  $R$  is related to the sheet conductivity by

$$\sigma_{4pp} = \frac{\ln 2}{\pi R}. \tag{1}$$

We obtained  $\sigma_{4pp}^{cap} = 1.3 \pm 0.2$  mS/ $\square$  for the Se-capped sample and  $\sigma_{4pp}^{noncap} = 1.2 \pm 0.1$  mS/ $\square$  for the noncapped sample, respectively. These two values coincide with each other within the measurement error, indicating that the quality of the film was not affected by the capping layer (and its removal procedure). These values of sheet conductivity are consistent with those of 8-quintuple-layer-thick  $\text{Bi}_2\text{Se}_3$  films grown on an  $\text{Al}_2\text{O}_3$  substrate: 1.3 mS/ $\square$  [26] and 1.9 mS/ $\square$  [27]. From the conductivity of bulk  $\text{Bi}_2\text{Se}_3$  [28],  $2 \times 10^5$  Sm $^{-1}$ , and the thickness of the  $\text{Bi}_2\text{Se}_3$  film, the sheet conductivity is estimated at 1.6 mS/ $\square$ , which is of the same order as that measured in this work. It should be the sum of the surface and the bulk conductivity, while the conductivity of an ultrathin film is often reduced by the restriction in the thickness direction.

Next, the conductivity of  $\text{Bi}_2\text{Se}_3$  wires fabricated with FIB  $\text{Ga}^+$  currents of 1 and 330 pA was measured. The result for wires of 3- and 2-  $\mu\text{m}$  width, etched out with a 1-pA FIB is shown in Fig. 6(b) for the capped and noncapped samples; the  $I$ - $V$  curves are shown in the inset. The resistance is proportional to the length  $L$  of the

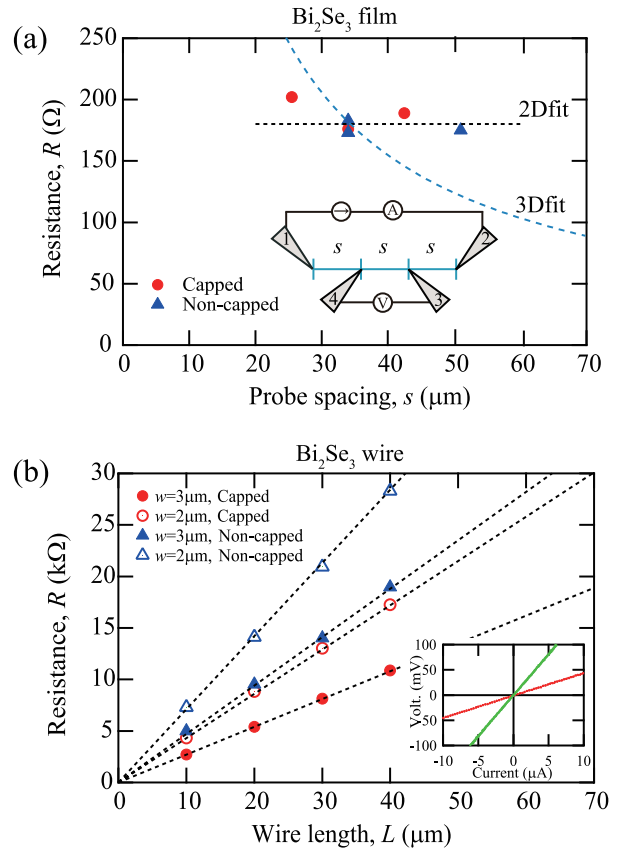


FIG. 6. (a) Resistance of  $\text{Bi}_2\text{Se}_3$  film measured by the linear four-point probe method as a function of the probe spacing  $s$  and the tip numbers are defined in the inset. The black and blue dashed lines are the fit for two- and three-dimensional conduction, respectively. (b) Resistance of the  $\text{Bi}_2\text{Se}_3$  wires fabricated by using a 1-pA  $\text{Ga}^+$  focused ion beam current, as a function of the length  $L$  between the voltage pads. The dotted lines are linear-fitting curves to the data of 3- and 2- $\mu\text{m}$ -wide wires of the capped or noncapped samples. The inset shows  $I$ - $V$  curves obtained in the measurement of the  $w = 2$   $\mu\text{m}$  capped wire (red for  $L = 10$   $\mu\text{m}$  and green for  $L = 20$   $\mu\text{m}$ , respectively).

measured portion, with different gradients depending on the wire width and the existence of the Se-capping layer. Similar results were obtained in the previous four-point probe measurement of nanowires of different materials self-assembled on Si surfaces [24, 29, 30]. The data in Fig. 6(b) can be fitted with straight lines according to

$$R = \rho_{1D} L = \frac{L}{\sigma_{1D}}, \tag{2}$$

where  $\rho_{1D}$  and  $\sigma_{1D}$  are one-dimensional (1D) resistivity and 1D (wire) conductivity, respectively. The results indicate that the applied current was confined within and passed through the wire only, without any leakage to the outer area of the  $\text{Bi}_2\text{Se}_3$  film or the substrate, implying that the insulation by the FIB-fabricated trenches was sufficient for controlling the current path. This should be expected since the trench resistance (on the order of M $\Omega$  as shown in Fig. 3) is much larger than the wire resistance (on the order of k $\Omega$ ).

Similar results were obtained for the noncapped samples (triangles in Fig. 6(b)). However, one can see that the

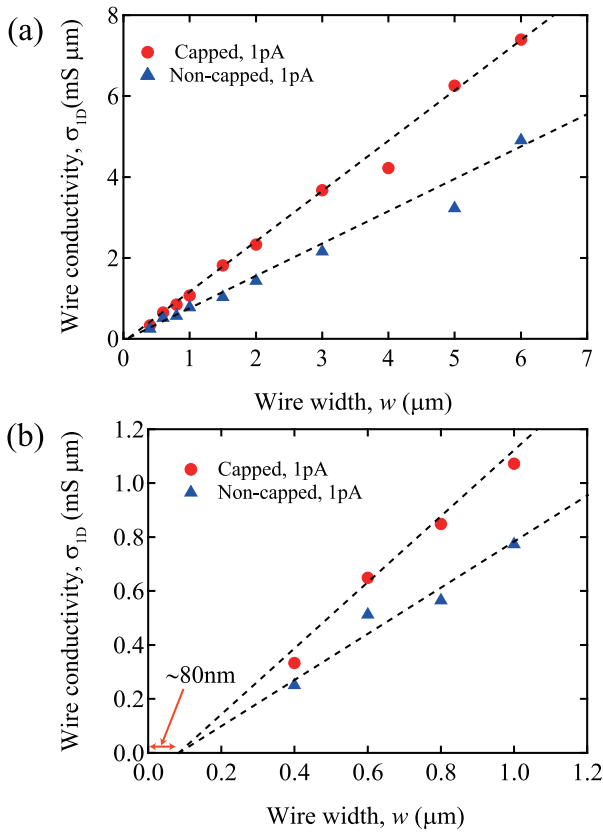


FIG. 7. (a) Wire conductivity of Bi<sub>2</sub>Se<sub>3</sub> wires as a function of the width for the samples fabricated by using a 1-pA Ga<sup>+</sup> focused ion beam current. The red circles and blue triangles indicate the values of the capped and noncapped samples, respectively. (b) Magnified presentation for smaller widths ( $w < 1 \mu\text{m}$ ).

one-dimensional resistance  $\rho_{1D}$  of the noncapped samples is always larger than that of the capped samples when wires of the same widths are compared. The same trend was true for the capped and noncapped wires fabricated by using the 330-pA FIB (not shown here). The reason for the difference in  $\rho_{1D}$  between the capped and noncapped samples will be discussed later.

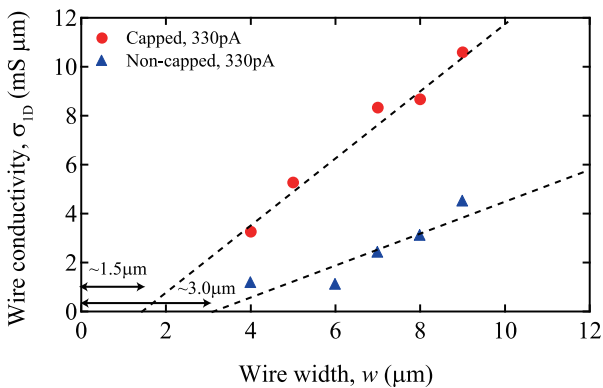


FIG. 8. Wire conductivity of Bi<sub>2</sub>Se<sub>3</sub> wires as a function of the wire width for the samples fabricated by using a 330-pA Ga<sup>+</sup> focused ion beam current. The red circles and blue triangles indicate the Se-capped and the noncapped samples, respectively. The arrows emphasize the intercepts.

Thus, the 1D resistivity  $\rho_{1D}$  varied systematically depending on the wire width. The wire conductivity  $\sigma_{1D}$ , which is the inverse of the 1D resistivity  $\rho_{1D}$ , for 1-pA- and 330-pA-FIB-fabricated samples is plotted as a function of the wire width  $w$  in Figs. 7 and 8, respectively. For both the capped and noncapped samples,  $\sigma_{1D}$  increases as the wire becomes wider. This corresponds to the results in Fig. 6(b), in which wider wires exhibit lower resistances. This is naturally explained by considering that an infinite film cut into a wire of width  $w$ ; the relation between the sheet conductivity of film  $\sigma_{2D}$  and the wire conductivity  $\sigma_{1D}$  can be written as

$$\sigma_{1D} = \sigma_{2D}w. \tag{3}$$

The wire conductivity is proportional to the wire width and the proportionality constant should equal the sheet conductivity of the original film, which should be compared with the measured sheet conductivity  $\sigma_{4pp}$  in Eq. (1). The sheet conductivity should be reproduced by linear fitting, as shown in Figs. 7(a) and (b). However, we have obtained better agreement between the experimental data and linear fitting by assuming a finite intercept on the horizontal axis in Fig. 7:

$$\sigma_{1D} = \sigma_{2D}(w - w_0), \tag{4}$$

where  $w_0$  represents some reduction in the effective width of the wire. The data obtained in this experiment for 1-pA-FIB-fabricated wires (Fig. 7) are reproduced best with  $\sigma_{2D}^{cap} = 1.26 \text{ mS}/\square$ ,  $\sigma_{2D}^{noncap} = 0.76 \text{ mS}/\square$ , and  $w_0 \sim 80 \text{ nm}$  (Figs. 7(a) and (b)). Indeed, the FIB-etched wires are thinner than the designed width because the trenches bordering both sides of the wire have a finite width. From the SIM observations, one sees that the trench width was about 100 nm, which roughly agreed with the width reduction  $w_0$  (Fig. 9(a)).

Another important aspect to note is that the value of  $\sigma_{2D}^{cap}$  is exactly the same as  $\sigma_{4pp}^{cap}$  obtained by using the linear four-point probe method on the unpatterned area of the film (Fig. 6(a)), whereas the value of  $\sigma_{2D}^{noncap}$  is about half of  $\sigma_{4pp}^{noncap}$ . This issue will be discussed later.

The same discussion is applicable to the data for 330-pA-FIB-fabricated samples. The sheet conductivity of the bare Bi<sub>2</sub>Se<sub>3</sub> film in the unpatterned area was  $\approx 1.3 \text{ mS}/\square$  by using the linear four-point probe measurement, which was the same as before. From the wires patterned with 330-pA-FIB etching, we obtained a value of  $\sigma_{2D}^{cap} = 1.4 \text{ mS}/\square$  from the slope in Fig. 8 for the capped sample, which is the same as the pristine sheet conductivity  $\sigma_{4pp}^{cap}$ . However, the conductivity for the wire from the non-capped sample exhibits a slope of nearly half that in Fig. 8, giving  $\sigma_{2D}^{noncap} = 0.7 \text{ mS}/\square$ , which is almost half of  $\sigma_{4pp}^{noncap}$ . The intercept  $w_0$  on the horizontal axis in Fig. 8 is much larger than that for the 1-pA-FIB etching in Fig. 7;  $w_0$  is about a few micrometers, which is a factor of 10 larger than that of 1-pA-FIB-etched samples. This large value of  $w_0$  cannot be explained by the diameter of the Ga<sup>+</sup> FIB. We found the same phenomenon not only in the Bi<sub>2</sub>Se<sub>3</sub> samples but also in the Bi sample. Fig. 10 shows the dependence of the conductivity on the wire width. The blue dotted line represents the wire conductivity estimated from the two-dimensional conductivity of the Bi film, which was measured by using the linear four-point probe method,  $3.39 \text{ mS}/\square$ . However, the

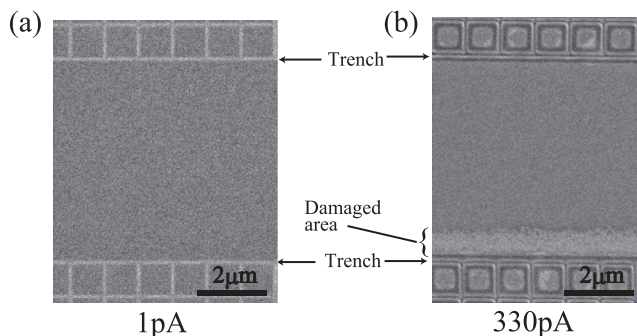


FIG. 9. SIM images of the  $\text{Bi}_2\text{Se}_3$  wires etched with (a) 1-pA and (b) 330-pA  $\text{Ga}^+$  focused ion beam currents, respectively.

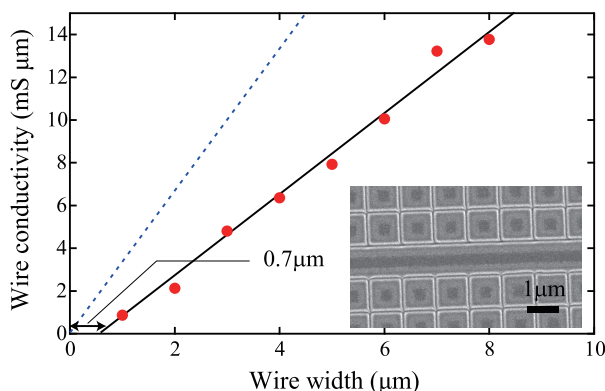


FIG. 10. Wire conductivity of Bi wires etched from a 20-bilayer-thick Bi film (without any capping layer) by using a 330-pA FIB for various wire widths. The black solid line is a linear fit to the data. The blue dotted line represents the wire conductivity estimated from the two-dimensional conductivity of the Bi film and the wire width. The inset is a SIM image of the 1- $\mu\text{m}$ -wide Bi wire.

actual wire conductivity is approximately half the estimated value. One can also recognize an intercept about 0.7  $\mu\text{m}$ . The length of the intercept corresponds to the damaged area, which looks brighter in the inset of Fig. 10. Another similar phenomenon is reported for GaAs wires etched out of a film by a FIB where the effective electrical width of the wire is reduced from the geometrical width [31]. Considering all these facts, we conclude that the reduction of conductivity and wire width is likely to be a general phenomenon in a system where FIB etching was performed.

#### IV. DISCUSSION

Two things are clearly shown by the data shown above:

- (A) The sheet conductivity of the  $\text{Bi}_2\text{Se}_3$  film obtained from the *wire measurements* is significantly reduced for the noncapped samples ( $\sigma_{2D}^{noncap}$ ) compared with the Se-capped samples ( $\sigma_{2D}^{cap}$ ), whereas the sheet conductivity measured in the unpatterned regions are the same irrespective of capping ( $\sigma_{4pp}^{cap}$  versus  $\sigma_{4pp}^{noncap}$ ).
- (B) The wire width for electrical conduction is significantly reduced effectively at the wires etched out by

a higher  $\text{Ga}^+$  beam current in FIB fabrication.

From (A) above, we can say that the  $\text{Bi}_2\text{Se}_3$  film near the FIB-etched area suffers some unintentional damage from the  $\text{Ga}^+$  beam, reducing the conductivity, and that such damage can be prevented by the Se-capping layer.

It is known that a typical  $\text{Ga}^+$  FIB profile is of Gaussian form and that the beam diameter is defined as its full width at half maximum. However, the Gaussian profile does not reproduce the beam intensity off the beam center: the intensity does not decay as fast as a Gaussian. This region is called *beam tail* and extends more than hundreds of nanometers away from the beam center even if the beam diameter is only 50 nm[32]. Less than 0.1% of the total beam current contributes to the beam tail, which is, however, shown to be enough to damage the atomic structure of graphene even 10  $\mu\text{m}$  away from the beam center[33]. In addition, it can be said that, on our  $\text{Bi}_2\text{Se}_3$  film etched without the Se capping layer, the trenches were etched right under the FIB beam center while the wire region near the trenches was irradiated by the beam tail. Some modifications, such as destruction of the crystal lattice and Ga ion implantation, may result from the irradiation of the beam tail, rather than sputtering on the wire region, because the beam tail is not intense enough for sputtering [23]. The tail damaged the  $\text{Bi}_2\text{Se}_3$  film in some way and led to the reduction of the  $\text{Bi}_2\text{Se}_3$  conductivity of the noncapped samples. The same is true in the Bi film case. On the capped samples, however, though the  $\text{Ga}^+$  beam tail irradiated and damaged the Se capping layer, the damage did not reach the  $\text{Bi}_2\text{Se}_3$  film underneath, so that the  $\text{Bi}_2\text{Se}_3$  film retained its quality and conductivity.

With respect to the result (B) above, Fig. 9 clearly shows the situation: The region on the  $\text{Bi}_2\text{Se}_3$  wire near the trench etched with the 330-pA  $\text{Ga}^+$  beam shows some damage within  $\approx 1 \mu\text{m}$  of the trench, as shown in Fig. 9(b), whereas that in the case of the 1-pA beam does not show any apparent damage, as shown in Fig. 9(a). The high beam current brings about an expansion of the beam diameter and an increase in intensity and extension of the tail of the  $\text{Ga}^+$  beam. Consequently, a wider region near the etched trench suffers the unintentional irradiation of the  $\text{Ga}^+$  beam, which is enough to damage the  $\text{Bi}_2\text{Se}_3$  film even beneath the Se capping layer. Note that the Se-capping layer cannot prevent this damage near the trench with the higher current (Fig. 9(b)), unlike in the case with a 1-pA beam (Fig. 9(a)). Therefore, a lower beam current is required when using a FIB to fabricate fine structures to reduce damage as much as possible.

#### V. SUMMARY

In summary, we have constructed a multichamber system, combined with molecular beam epitaxy, FIB micro-fabrication, and electrical measurements by using a four-tip STM, that enables *in situ* fabrication and electrical measurements in UHV while preserving the surface structures of samples. We measured the electrical conduction of  $\text{Bi}_2\text{Se}_3$  wires that were FIB-etched out of  $\text{Bi}_2\text{Se}_3$  ultrathin films epitaxially grown on Si(111) substrate. The dependencies of the resistance on the length of wire un-

der measurement and the wire width exhibited a one-dimensional character, indicating that the measurement current was confined within and passed through the wire without any leakage. The trenches bordering the wire worked as insulating barriers. We also studied the influence of radiation damage caused by FIB etching on the conductivity of Bi<sub>2</sub>Se<sub>3</sub> wires, finding that an amorphous Se layer serves as a mask and can be removed easily to recover the pristine Bi<sub>2</sub>Se<sub>3</sub> surface. Unintentional irradiation of the tail of the Ga<sup>+</sup> beam in the FIB may be the cause of the damage, though it can be avoided by covering the sample surface with a Se-capping layer before the FIB etching. Although all the fabrication processes were done *in situ* in UHV without exposing the samples to air in the present experiment, we needed to be very careful about the unintentional irradiation of the Ga<sup>+</sup> beam in FIB fabrication to maintain the intrinsic properties of the surface.

When a high Ga<sup>+</sup> beam current was used in FIB fabrication, another kind of damage was observed near the etched trenches, resulting in the reduction of the effective width of wire for electrical transport. Although this dam-

age cannot be avoided by using the Se-capping layer, it can be reduced by using a lower Ga<sup>+</sup> beam current.

Although we need to be very careful about the damage caused by FIB fabrication, the present results suggest possible applications of the *in situ* FIB technique to studies on surface-state electron transport. By restricting the current paths within characteristic lengths of the system, such as the carrier mean free path and spin diffusion length, we will be able to explore quantum transport at surfaces in versatile ways.

## ACKNOWLEDGMENTS

The present work has been supported by the Grants-in-Aid for Scientific Research Program from the Japan Society for the Promotion of Science and by the New Academic Field “Molecular Architectonics” of the Ministry of Education, Culture, Sports, Science and Technology.

- 
- [1] T. Aruga, Surf. Sci. Rep. **61**, 283 (2006).  
 [2] H. W. Yeom, *et al.*, Phys. Rev. Lett. **82**, 4898 (1999).  
 [3] P. S. Snijders and H. H. Weitering, Rev. Mod. Phys. **82**, 307 (2010).  
 [4] T. Hirahara, T. Nagao, I. Matsuda, G. Bihlmayer, E. V. Chulkov, Yu. M. Koroteev, P. M. Echenique, M. Saito, and S. Hasegawa, Phys. Rev. Lett. **97**, 146803 (2006).  
 [5] C. R. Ast, J. Henk, A. Ernst, L. Moreschini, M. C. Falub, D. Palicé, P. Bruno, K. Kern, and M. Grioni, Phys. Rev. Lett. **98**, 186807 (2007).  
 [6] K. Sakamoto, H. Kakuta, K. Sugawara, K. Miyamoto, A. Kimura, T. Kuzumaki, N. Ueno, E. Annese, J. Fujii, A. Kodama, T. Shishidou, H. Namatame, M. Taniguchi, T. Sato, T. Takahashi, and T. Oguchi, Phys. Rev. Lett. **103**, 156801 (2009).  
 [7] H. Zhang, C.-X. Liu, X.-L. Qi, X. Dai, Z. Fang, and S.-C. Zhang, Nat. Phys. **5**, 438 (2009).  
 [8] Y. Xia, D. Qian, D. Hsieh, L. Wray, A. Pal, H. Lin, A. Bansil, D. Grauer, Y. S. Hor, R. J. Cava, and M. Z. Hasan, Nat. Phys. **5**, 398 (2009).  
 [9] D. Hsieh, D. Qian, L. Wray, Y. Xia, Y. S. Hor, R. J. Cava, and M. Z. Hasan, Nature **452**, 970 (2008).  
 [10] S. Hasegawa, X. Tong, S. Takeda, N. Sato, T. Nagao, Prog. Surf. Sci. **60**, 89 (1999).  
 [11] S. Heike, S. Watanabe, Y. Wada, and T. Hashizume, Phys. Rev. Lett. **81**, 890 (1998).  
 [12] T. Hirahara, I. Matsuda, S. Yamazaki, N. Miyata, S. Hasegawa, and T. Nagao, Appl. Phys. Lett. **91**, 202106 (2007).  
 [13] S. Yamazaki, Y. Hosomura, I. Matsuda, R. Hobara, T. Eguchi, Y. Hasegawa, and S. Hasegawa, Phys. Rev. Lett. **106**, 116802 (2011).  
 [14] T. Kanagawa, R. Hobara, I. Matsuda, T. Tanikawa, A. Natori, and S. Hasegawa, Phys. Rev. Lett. **91**, 036805 (2003).  
 [15] Ph. Hofmann and J. W. Wells, J. Phys.: Condens. Matter **21**, 013003 (2009).  
 [16] C. Tegenkamp, Z. Kallassy, H. Pfürer, H.-L. Günter, V. Zielasek, and M. Henzler, Phys. Rev. Lett. **95**, 176804 (2005).  
 [17] T. Uchihashi, P. Mishra, M. Aono, and T. Nakayama, Phys. Rev. Lett. **107**, 207001 (2011).  
 [18] L. D. Menard and J. M. Ramsey, Nano Lett. **11**, 512 (2011).  
 [19] Y. N. Picard, D. P. Adams, M. J. Vasile, and M. B. Ritchey, Precision Eng. **27**, 59 (2003).  
 [20] R. Hobara, N. Nagamura, S. Hasegawa, I. Matsuda, Y. Yamamoto, K. Ishikawa, and T. Nagamura, Rev. Sci. Instrum. **78**, 053705 (2007).  
 [21] G. Zhang, H. Q. Teng, J. Guo, Q. Guo, X. Dai, Z. Fang, and K. Wu, Appl. Phys. Lett. **95**, 053114 (2009).  
 [22] Y. Sakamoto, T. Hirahara, H. Miyazaki, S.-i. Kimura, and S. Hasegawa, Phys. Rev. B **81**, 165432 (2010).  
 [23] L. Frey, C. Lehrer, H. Rysse, Appl. Phys. A **76**, 1017 (2003).  
 [24] M. R. Kaspers, A. M. Bernhart, F.-J. Meyer zu Heringdorf, G. Dumpich, and R. Möller, J. Phys.: Condens. Matter **21**, 265601 (2009).  
 [25] S. Hasegawa, I. Shiraki, F. Tanabe, and R. Hobara, Current Appl. Phys. **2**, 465 (2002).  
 [26] A. A. Taskin, S. Sasaki, K. Segawa, and Y. Ando, Phys. Rev. Lett. **109**, 066803 (2012).  
 [27] N. Bansal, Y. S. Kim, M. Brahlek, E. Edrey, and S. Oh, Phys. Rev. Lett. **109**, 116804 (2012).  
 [28] G. R. Hyde, H. A. Beale, and I. L. Spain, J. Phys. Chem. Solids, **35**, 1719-1728 (1974).  
 [29] H. Okino, I. Matsuda, R. Hobara, Y. Hosomura, S. Hasegawa, and P. A. Bennett, Appl. Phys. Lett. **86**, 233108 (2005).  
 [30] S. Yoshimoto, Y. Murata, K. Kubo, K. Tomita, K. Motoyoshi, T. Kimura, H. Okino, R. Hobara, I. Matsuda, S. Honda, M. Katayama, and S. Hasegawa, Nano Lett. **7**, 956 (2007).  
 [31] T. Hiramoto, K. Hirasawa, Y. Iye, and T. Ikoma, Appl. Phys. Lett. **51**, 1620 (1987).  
 [32] A. Kieslich, J. P. Reithmaier, A. Forchel, J. Vac. Sci. Technol. B **12**, 3518 (1994).  
 [33] B. S. Archanjo, A. P. M. Barboza, B. R. A. Neves, L. M. Malard, E. H. M. Ferreira, J. C. Brant, E. S. Alves, F. Plentz, V. Carozo, B. Fragneaud, I. O. Maciel, C. M. Almeida, A. Jorio, and C. A. Achete, Nanotechnology **23**, 255305 (2012).